Vibrations of beams and rods carrying a moving mass

2016 J. Phys.: Conf. Ser. 721 012016

(http://iopscience.iop.org/1742-6596/721/1/012016)

Vibrations of beams and rods carrying a moving mass

X W Zhao[1,2], G H M van der Heijden[1], Z D Hu[2]

[1] Department of Civil, Environmental & Geomatic Engineering, University College London, London, UK,

[2] School of Aerospace Engineering and Applied Mechanics, Tongji University, Shanghai, People's Republic of China

E-mail: xingwei.zhao@ucl.ac.uk, g.heijden@ucl.ac.uk, zdhu@tongji.edu.cn

Abstract. We study the vibration of slender one-dimensional elastic structures (beams, cables, wires, rods) under the effect of a moving mass or load. We first consider the classical small-deflection (Euler-Bernoulli) beam case, where we look at tip vibrations of a cantilever as a model for a barreled launch system. Then we develop a theory for large deformations based on Cosserat rod theory. We illustrate the effect of moving loads on large-deformation structures with a few cable and arch problems. Large deformations are found to have a resonance detuning effect on the cable. For the arch we find different failure modes depending on its depth: a shallow arch fails by in-plane collapse, while a deep arch fails by sideways flopping. In both cases the speed of the traversing load is found to have a stabilising effect on the structure, with failure suppressed entirely at sufficiently high speed.

1. Introduction

The problem of a continuously distributed system carrying a moving concentrated mass has broad applications in mechanics and engineering, including space tethers, satellite antennas, launch systems, robotic arms [1], cranes, flexible manipulators [2], high-speed train railroads and highway bridges with moving vehicles [3]. For an overview of the sizable early literature on the vibration theory of moving mass and load problems we refer to Fryba's monograph [4].

The classical example of a moving mass problem is the idealisation of a vehicle-bridge system. In this case the moving vehicle is usually treated as a moving force, or load, of constant magnitude, while the bridge is modelled as a simply-supported beam. This problem is therefore more accurately described as a moving load problem [3]. The moving load assumption does not take into account the inertial forces of the moving mass and of the interactions between the moving mass and the continuous beam. The moving load treatment is therefore insufficient when the gravitational and inertial effects of the moving mass are not negligible compared to the mass of the structure. In [5] it was shown that the moving load solution is not an upper bound for the moving mass solution for the (simply-supported and clamped-clamped) boundary conditions considered there.

Ting et al. [6] were among the first to consider the inertial forces, including centrifugal and Coriolis effects, of the moving mass as an interaction between the mass and the beam. Further studies of the moving mass problem include [7, 8, 9]. All these works restrict themselves to beams undergoing small deformations (in [8] moderately large deflections are considered) and all consider only two-dimensional bending vibrations. With the current drive to use thinner and lighter materials, in order to save material and reduce costs, large deformations become increasingly important.

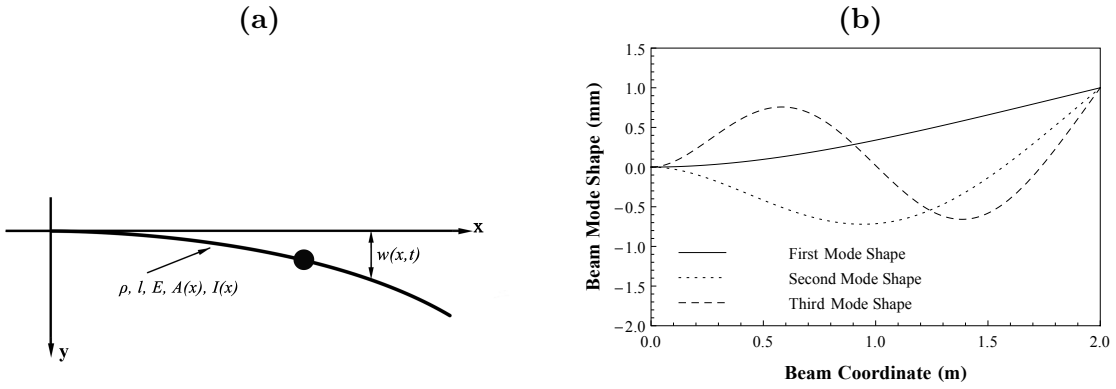

Figure 1. (a) Cantilever beam carrying a moving mass. (b) The first three mode shapes of the cantilever beam.

This paper first briefly reviews the small-deformation theory and then presents early results of our programme to develop a theory for slender elastic rods undergoing arbitrary deformations (under small strains) while carrying a moving load or mass. The small-deformation beam case is motivated by launch systems and studies the effects of a moving mass on the tip vibration of a cantilever beam, important for the projectile motion of the released mass. We have previously considered tapered beams [10], but here consider beams with uniform (circular) cross-section. The large-deformation rod case is motivated by cable-mass systems. We show some preliminary results in which a load (weight) traverses a cable or arch at constant speed, as is customary in the classical small-deformation case. Such prescribed motion of the mass will be unrealistic in certain application and a full large-deformation theory will ultimately have to describe the two-way coupling between rod and mass: the mass affects the deformation of the rod but the deformed rod will also affect the speed of the mass as it is forced to track the shape of the rod (under gravity). This is work in progress.

2. Beam with a moving mass

The beam is assumed to undergo small deflections. We can then write $x(t)$ for the position of the mass along the axis of the beam and $w(x(t),t)$ for the position of the mass in space (see Fig. 1(a)). The vertical velocity and acceleration of the moving mass are then computed as

$$\frac{\mathrm{d}w}{\mathrm{d}t} = v(t)\frac{\partial w}{\partial x} + \frac{\partial w}{\partial t}, \qquad \frac{\mathrm{d}^2w}{\mathrm{d}t^2} = v^2(t)\frac{\partial^2 w}{\partial x^2} + 2v(t)\frac{\partial^2 w}{\partial x \partial t} + a(t)\frac{\partial w}{\partial x} + \frac{\partial^2 w}{\partial t^2}. \tag{1}$$

The first and second terms of the acceleration are the centrifugal and Coriolis terms, respectively.

We model the beam as an Euler-Bernoulli beam. The action functional for use in Hamilton's principle is

$$S = \int_{t_1}^{t_2} \left\{ \int_0^L \left[\frac{1}{2}\rho A(x) \left(\frac{\partial w}{\partial t}\right)^2 - \frac{1}{2} EI(x) \left(\frac{\partial^2 w}{\partial x^2}\right)^2 + \rho A(x) g w \right] \mathrm{d}x + \frac{1}{2} M \left(\frac{\mathrm{d}w}{\mathrm{d}t}\right)^2 + Mgw \right\} \mathrm{d}t. \tag{2}$$

Here L is the length, ρ the density, A the cross-sectional area, I the second moment of area about the z-axis and E Young's modulus. The mass M slides along the length of the beam with local speed $v(t)$ and acceleration $a(t)$.

We use a Galerkin approximation to spatially discretise the problem and write the beam deflection as a truncated series $w(x,t) = \sum_{i=1}^{n} \Phi_i(x) Y_i(t)$, where the $\Phi_i(x)$ are (the first n) mode shapes of the free beam and the $Y_i(t)$ are time-dependent dimensionless coefficients. After

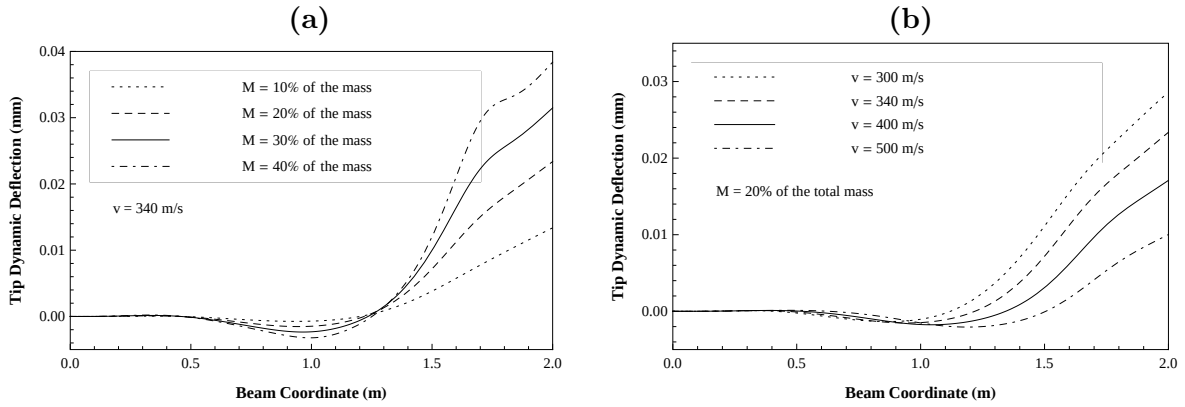

Figure 2. (a) Tip deflections at various values of M for different travelling velocities v. The 'beam coordinate' is the instantaneous position along the beam of the travelling mass. (b) Tip deflections at various values of v for different travelling masses M.

substitution of this series expansion into Eq. (2) the integrand of S becomes a function of Y_i and $\dot{Y}_i$ and the application of Hamilton's principle gives the Euler-Lagrange equations in the form

$$\mathbf{M}(t)\ddot{\mathbf{Y}}(t) + \mathbf{C}(t)\dot{\mathbf{Y}}(t) + \mathbf{K}(t)\mathbf{Y}(t) = \mathbf{P}(t), \tag{3}$$

where $\mathbf{Y}(t) = [Y_1(t), Y_2(t), \ldots, Y_n(t)]^T$ and $\mathbf{M}$, $\mathbf{K}$ and $\mathbf{C}$ are the mass, stiffness and 'damping' matrices, respectively (note that $\mathbf{C}$ comes from the Coriolis effect of the moving mass and is antisymmetric and therefore does not actually represent damping in the sense that there is no dissipation). $\mathbf{M}$ is symmetric but $\mathbf{K}$ varies with the beam coordinate $x(t)$ as the mass moves along the beam and as a result is nonsymmetric. $\mathbf{P}$ is the load vector (due to gravity).

Fig. 1(b) shows the first three mode shapes of the cantilever beam. Here we have used the normalisation that the absolute tip deflections $|\Phi_i(L)|$ are 1.

Example. We consider a hollow steel beam ($E = 2.0 \times 10^{11}\,\mathrm{Pa}, \rho = 7850\,\mathrm{kg/m^3}$) of length $L = 2\,\mathrm{m}$, outer radius $R = 0.1\,\mathrm{m}$ and inner radius $r = 0.05\,\mathrm{m}$. The magnitude (M) and the (uniform) speed (v) of the moving mass will be varied. We focus on the effect of these parameters on beam tip and mass deflections as the beam is excited by the travelling mass. We take initial conditions where the mass starts moving when the beam is in the static equilibrium configuration and compute expansions of the beam deflection in terms of the first three mode shapes Φ_i, i.e., we take $n = 3$.

Solutions, obtained using the fourth-order Runge-Kutta method, are given in the dynamic tip deflection plots of Fig. 2 for four different velocities v and for four different values of M, specified as the percentage of the total mass of the beam-mass system. In each plot the tip deflection $w(L,t)$ of the beam is given as a function of the instantaneous position $x(t)$ of the moving mass. We call this the beam coordinate. Since the speed is constant it can be interpreted as a time coordinate. When $x(t) = L = 2$, the mass has reached the end of the beam.

We find that for the parameters used the tip vibrations are very small. At relatively high speeds the mass movement triggers the beam tip to vibrate. Generally, the higher the speed v and the larger the mass M, the higher the vibration frequency of the beam tip. The amplitude of delfection reduces as the speed v increases.

3. Large deformations – Cosserat rod formulation

Let $\boldsymbol{r}(s,t) : [0, L] \times \mathbb{R} \to \mathbb{R}^3$ be a smooth space curve of length L describing the centerline of the rod. Further, let $\{\boldsymbol{d}_1(s,t), \boldsymbol{d}_2(s,t), \boldsymbol{d}_3(s,t)\}$ be a frame of orthonormal directors such that $\boldsymbol{d}_1$

and $\boldsymbol{d}_2$ span the cross-section of the rod, pointing in its principal directions, and $\boldsymbol{d}_3 = \boldsymbol{d}_1 \times \boldsymbol{d}_2$ is perpendicular to it. Orthonormality of the frame implies the existence of two axial vectors $\boldsymbol{\kappa}$ (the curvature vector) and $\boldsymbol{\omega}$ (the spin vector) such that

$$\partial_s \boldsymbol{d}_k = \boldsymbol{\kappa} \times \boldsymbol{d}_k, \qquad \partial_t \boldsymbol{d}_k = \boldsymbol{\omega} \times \boldsymbol{d}_k \qquad (k = 1, 2, 3). \tag{4}$$

The force and moment equilibrium equations are given by

$$\partial_s \boldsymbol{n} + \boldsymbol{f} = \rho A \partial_{tt} \boldsymbol{r}, \qquad \partial_s \boldsymbol{m} + \partial_s \boldsymbol{r} \times \boldsymbol{n} + \boldsymbol{l} = \rho \partial_t (\boldsymbol{I}\boldsymbol{\omega}), \tag{5}$$

where $\boldsymbol{n}$ and $\boldsymbol{m}$ are the resultant contact force and contact couple acting at the centreline at s, and $\boldsymbol{f}$ and $\boldsymbol{l}$ are external forces and moments acting on the rod [11]. $\boldsymbol{I}$ is the moment of inertia tensor, A is the area of the cross-section and ρ is the density.

We take the rod to be inextensible and unshearable. Then the director $\boldsymbol{d}_3$ coincides with the tangent to the centreline of the rod, i.e., $\partial_s \boldsymbol{r} = \boldsymbol{d}_3$. If we also introduce the centreline velocity $\boldsymbol{u} = \partial_t \boldsymbol{r}$, then the identity $\partial_t \partial_s \boldsymbol{r}(s,t) = \partial_s \partial_t \boldsymbol{r}(s,t)$ can be written as

$$\partial_t \boldsymbol{d}_3 = \partial_s \boldsymbol{u}. \tag{6}$$

Similarly, the identity $\partial_t \partial_s \boldsymbol{d}_k(s,t) = \partial_s \partial_t \boldsymbol{d}_k(s,t)$, on using Eq. (4), leads to the curvature-spin compatibility equation

$$\partial_s \boldsymbol{\omega} = \partial_t \boldsymbol{\kappa} + \boldsymbol{\kappa} \times \boldsymbol{\omega}. \tag{7}$$

When expressed in the director frame, Eqs (5), (6), (7) give us the following equations (using a sans-serif font for triples of components and denoting $\boldsymbol{I}$ on principal axes by $\mathsf{I} = \mathrm{diag}(I_1, I_2, J)$):

$$\begin{aligned} \rho A \partial_t \mathsf{u} &= \partial_s \mathsf{n} + \kappa \times \mathsf{n} - \rho A(\omega \times \mathsf{u}) + \mathsf{f}, \\ \rho \mathsf{I} \partial_t \omega &= \partial_s \mathsf{m} + \kappa \times \mathsf{m} + \mathsf{d}_3 \times \mathsf{n} - \rho(\omega \times \mathsf{I}\omega) + \mathsf{l}, \\ \partial_t \kappa &= \partial_s \omega + \kappa \times \omega, \\ \mathsf{0} &= \partial_s \mathsf{u} + \kappa \times \mathsf{u} - \omega \times \mathsf{d}_3. \end{aligned} \tag{8}$$

We finally introduce linear constitutive relations between the curvatures κ and the (body) moments m: $\mathsf{m} = \bar{\mathsf{K}}\kappa$, where $\bar{\mathsf{K}} = \mathrm{diag}(B_1, B_2, C)$, with $B_1 = EI_1$ and $B_2 = EI_2$ the principal bending stiffnesses and $C = GJ$ the torsional stiffness, E and G being Young's modulus and the shear modulus respectively. These relations can be used to eliminate m in Eq. (8) in favour of κ, thus giving us 12 equations for the body components $(\mathsf{u}, \omega, \kappa, \mathsf{n}) =: \boldsymbol{y}$ in the form

$$\boldsymbol{M}\partial_t \boldsymbol{y}(s,t) + \boldsymbol{K}\partial_s \boldsymbol{y}(s,t) + \boldsymbol{F}(s,t) = \boldsymbol{0}, \tag{9}$$

where $\boldsymbol{M}$ and $\boldsymbol{K}$ are mass and stiffness matrices (constant in the case of a uniform rod). All nonlinear terms in Eq. (8) are contained in the load vector $\boldsymbol{F}$. The same formulation is used in [12, 13].

To solve the equations numerically we apply the generalised α-method [14] for both spatial and temporal discretisation. This yields the discrete form of Eq. (9) as follows:

$$\begin{aligned} &\boldsymbol{M}\{(1-\alpha_t)[(1-\alpha_s)\partial_t \boldsymbol{y}_j^i + \alpha_s \partial_t \boldsymbol{y}_{j-1}^i] + \alpha_t[(1-\alpha_s)\partial_t \boldsymbol{y}_j^{i-1} + \alpha_s \partial_t \boldsymbol{y}_{j-1}^{i-1}]\} \\ &\quad + \boldsymbol{K}\{(1-\beta_t)[(1-\beta_s)\partial_s \boldsymbol{y}_j^i + \beta_s \partial_s \boldsymbol{y}_{j-1}^i] + \beta_t[(1-\beta_s)\partial_s \boldsymbol{y}_j^{i-1} + \beta_s \partial_s \boldsymbol{y}_{j-1}^{i-1}]\} \\ &\quad + \{(1-\beta_t)[(1-\beta_s)\boldsymbol{F}_j^i + \beta_s \boldsymbol{F}_{j-1}^i] + \beta_t[(1-\beta_s)\boldsymbol{F}_j^{i-1} + \beta_s \boldsymbol{F}_{j-1}^{i-1}]\} = \boldsymbol{0}. \end{aligned} \tag{10}$$

In this equation the superscript indicates the time step while the subscript indicates the spatial step, i.e., the node of the discretised curve. The s and t derivatives are approximated as

$$\partial_t \boldsymbol{y}^i = \frac{\boldsymbol{y}^i - \boldsymbol{y}^{i-1}}{\gamma_t \Delta t} - \frac{1-\gamma_t}{\gamma_t}\partial_t \boldsymbol{y}^{i-1}, \qquad \partial_s \boldsymbol{y}_j = \frac{\boldsymbol{y}_j - \boldsymbol{y}_{j-1}}{\gamma_s \Delta s} - \frac{1-\gamma_s}{\gamma_s}\partial_s \boldsymbol{y}_{j-1}, \tag{11}$$

where Δs and Δt are the spatial step and time step, respectively. The six numerical parameters α_s, β_s, γ_s and α_t, β_t, γ_t can be tuned to obtain desirable accuracy and stability properties. We choose the value $1/2$ for all six parameters, which gives a stable second-order scheme without numerical damping. The final system of algebraic equations is solved with the global Newton code NLEQ1 [15].

To compute rod shapes in space we need to postprocess the solution $\boldsymbol{y}$ by subsequently solving either of the equations in (4) and integrating the centreline equation $\partial_s \boldsymbol{r} = \boldsymbol{d}_3$ or the velocity $\boldsymbol{u} = \partial_t \boldsymbol{r}$ to obtain $\boldsymbol{r}$. Let $\{\boldsymbol{i}, \boldsymbol{j}, \boldsymbol{k}\}$ be a fixed coordinate frame in space. We define R as the matrix whose columns are the frame vectors $\boldsymbol{i}$, $\boldsymbol{j}$, $\boldsymbol{k}$ represented in the body frame. R is thus the rotation matrix from the inertial to the body frame. Assuming we choose to use the second equation in (4) (i.e., time integration), the rotation matrix is updated according to

$$R(t + \Delta t) = e^{-\hat{\omega}\Delta t} R(t), \tag{12}$$

with initial condition $R(0) = I$ if the body frame at $t = 0$ is aligned with the fixed frame [16]. Here, $\hat{\omega}$ is the usual skew-symmetric matrix corresponding to the axial vector ω. The exponential is conveniently computed by using the Rodrigues formula (valid for any skew-symmetric matrix $\hat{\mathsf{x}}$)

$$e^{-\hat{\mathsf{x}}} = I - \hat{\mathsf{n}} \sin|\mathsf{x}| + \hat{\mathsf{n}}^2(1 - \cos|\mathsf{x}|), \qquad \mathsf{n} = \frac{\mathsf{x}}{|\mathsf{x}|}. \tag{13}$$

Having found R, we finally obtain the centreline $\boldsymbol{r}$ by integrating the velocity vector:

$$\partial_t \boldsymbol{r} = \boldsymbol{u} = R^{\mathrm{T}} \mathsf{u}. \tag{14}$$

The integrations in these postprocessing steps are carried out using the trapezoidal rule to maintain second-order accuracy.

The rotation matrix R is also used to transform any external forces or moments specified in the fixed frame (for instance gravity) to the body frame for inclusion in Eq. (8):

$$\mathsf{f} = R\boldsymbol{f}, \qquad \mathsf{l} = R\boldsymbol{l}. \tag{15}$$

Boundary conditions, if specified in the fixed frame, may similarly be transformed to the body frame.

4. Applications

We apply our formulation to a few structures that are initially planar but may suffer out-of-plane instabilities under the action of a moving point load F. We orient our fixed coordinate system $\{\boldsymbol{i}, \boldsymbol{j}, \boldsymbol{k}\}$ such that $\boldsymbol{j}$ is pointing vertically up, $\boldsymbol{k}$ is pointing horizontally along the end-to-end axis of the rod (in the direction of increasing s) and $\boldsymbol{i}$ is pointing out of the plane of the rod. We denote the components of the centreline of the rod, $\boldsymbol{r}$, in this fixed frame by (x, y, z) and choose the left end point to be at $(x, y, z) = (0, 0, 0)$. The external loads are gravity and the (vertical) moving load F, so we set $\mathsf{f} = -(\rho A g + F)\mathsf{j} = -(\rho A g + F) R\boldsymbol{j}$ and $\mathsf{l} = \mathsf{0}$ in Eq. (8), where g is the gravitational acceleration.

In all the following examples the rod is taken to be uniform, of length $L = 1\,\mathrm{m}$ and radius $r = 0.005\,\mathrm{m}$, while $E = 2.5 \times 10^8\,\mathrm{Pa}$, $\rho = 1500\,\mathrm{kg/m^3}$ and $g = 9.8\,\mathrm{m/s^2}$.

4.1. Hanging cable

Consider a cable hanging under gravity. Its end tangents are horizontal and prevented from rotation but the right end is free to move along the end-to-end axis (see true views in Figs 3(a) and (c)). At time $t = 0$ a vertical load of magnitude F starts to travel from the left to the right end with constant speed $v = \mathrm{d}\sigma/\mathrm{d}t$, where σ is the time-like 'rod coordinate', i.e., the

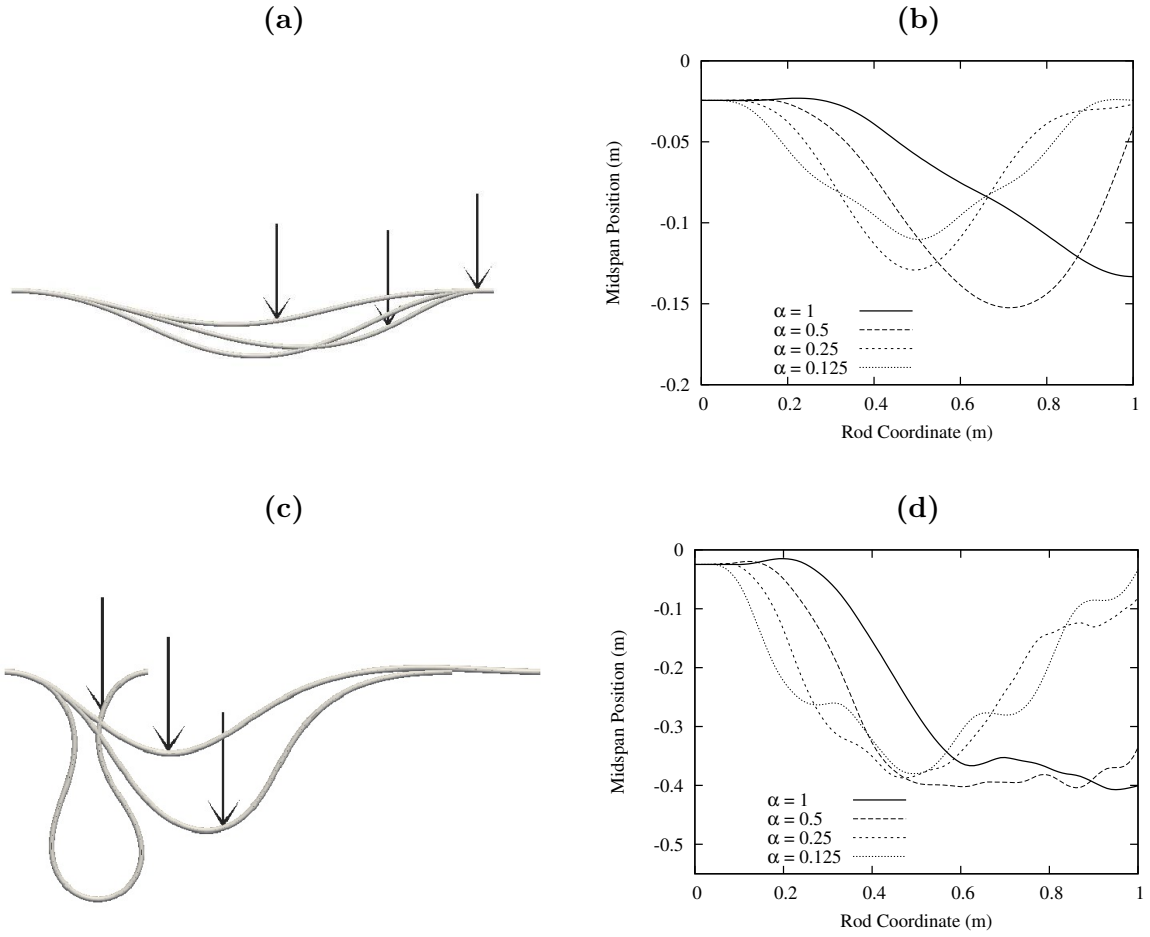

Figure 3. Cable shapes and vertical midspan positions for two different loads F moving at various speeds v given as a fraction α of the critical speed: (a,b) small load, $F = 2.0\,\mathrm{N}$; (c,d) large load, $F = 20.0\,\mathrm{N}$.

instantaneous arclength position of the travelling load. This, for instance, models the motion of inspection robots along bridge cables or high-voltage power lines [17]. We consider two cases: a small load ($F = 2.0\,\mathrm{N}$) and a large load ($F = 20.0\,\mathrm{N}$). Good numerical results are obtained by taking $\Delta s = 0.01$ and $\Delta t = \Delta s/v$, the latter having the effect that the cable solution is sampled at times when the load is applied exactly at a node.

Fig. 3 shows oscillations in the cable's vertical midspan position $y(L/2)$ plotted against the rod coordinate σ for various speeds v given as a fraction α of the first critical speed v_1. For small vibrations this critical speed is the speed required to cross the cable in half a period of its first bending mode, i.e., $v_1 = \omega_1 L/\pi$, where for fixed-fixed boundary conditions the first natural frequency ω_1 is given by $\omega_1 = (4.7300/L)^2\sqrt{EI/\rho A}$. We observe that in the case of a small load (Fig. 3(a,b)) there is a resonance phenomenon in the sense that the maximum amplitude of vibrations occurs for speeds near the resonance speed ($\alpha = 1$). The rod effectively behaves as a stiff beam and the results agree with those for an Euler-Bernoulli beam found in [18]. In the case of a large load (Fig. 3(c,d)) we observe a significant detuning effect: the rod behaves as a flexible cable with no resonance effect shown. The dimensionless parameter controlling the effective stiffness/flexibility of the loaded cable is EI/FL^2.

4.2. Hinged arch

Next we consider a constant vertical load traversing an arch. The initial arch is formed by buckling (upwards) an initially straight hinged-hinged rod under a quasistatically increasing compressive horizontal end load. The end-to-end distance is then fixed and gravity is 'switched on' by gradually increasing g from 0 to $9.8\,\mathrm{m/s^2}$ (the end force $\boldsymbol{n}(L)\cdot\boldsymbol{k}$ varies passively in this process). We do these initial parameter continuations with a separate statics code, so at this point we have a pure statics solution with all velocities and angular velocities equal to zero. We consider two types of arch, a shallow and a deep one. The shallow arch has its end-to-end distance fixed at $\Delta z = 0.864545\,\mathrm{m}$ and carries a load $F = 2.0\,\mathrm{N}$, while the deep arch has end-to-end distance $\Delta z = 0.529689\,\mathrm{m}$ and carries a load $F = 3.8\,\mathrm{N}$. The two arches have different failure modes under these loads when applied statically, as illustrated in Fig. 4: the shallow arch fails by in-plane collapse (described by the fold in the figure), while the deep arch fails by out-of-plane sideways flopping (described by a pitchfork bifurcation, which is followed by a restabilising reverse pitchfork bifurcation).

Instead of the static load we now consider dynamic loading, letting F move from the left end with constant speed v. Results are shown in Figs 5–7. In Fig. 5, for the shallow arch, we see that for small speed v the arch fails close to the point of quasistatic collapse, while at larger v collapse is significantly delayed and for speeds larger than $v = 2.6\,\mathrm{m/s}$ no collapse occurs at all. As a measure for this collapse we show in Fig. 5(a) the angular velocity $\boldsymbol{\omega}(L)\cdot\boldsymbol{i}$ about the hinge at $s = L$: its value first stays small as the load moves to the right and then suddenly goes sharply negative (corresponding to a rapid clockwise rotation of the right end tangent) as the arch snaps under the load. Shapes for $v = 0.5\,\mathrm{m/s}$ are shown in Fig. 5(b). Fig. 5(c) illustrates how the discontinuity in the internal force, as a result of the point load F, travels along the rod. Our numerical scheme has no problem with these discontinuities. Fig. 5(d) illustrates the stabilising effect of large v: for $v = 2.6\,\mathrm{m/s}$ the arch still significantly deforms under the travelling load, but no sudden jump occurs and the right end tangent does not change sign, while for $v = 20\,\mathrm{m/s}$ the arch deforms hardly at all under the moving load. The numerical parameters used in these shallow-arch runs are: $\Delta s = 0.00125$ for $v = 0.02$ and $\Delta s = 0.01$ for all other speeds, and again $\Delta t = \Delta s/v$.

Fig. 6, for the deep arch, shows that for sufficiently small speed v the arch goes unstable close to the point of quasistatic instability, with the arch oscillating about the stable out-of-plane statics solution (Fig. 6(a,b) for $v = 0.005\,\mathrm{m/s}$). For larger v the instability is somewhat delayed and oscillations are about the planar solution only (Fig. 6(c,d) for $v = 0.01\,\mathrm{m/s}$), although still of the same amplitude. This amplitude goes down as the speed v is increased further, as illustrated in Fig. 7, where the lateral displacement is tiny. We see again, as in the case of the shallow arch, but now for a completely different failure mode, that speed of the travelling load has a stabilising effect. A few shapes for the swaying arch are given in Fig. 8. The numerical parameters used in these deep-arch runs are: $\Delta s = 0.001$ for $v = 0.005$, $\Delta s = 0.00125$ for $v = 0.01$, $\Delta s = 0.002$ for $v = 0.05$, $\Delta s = 0.00125$ for $v = 0.1$, and $\Delta t = \Delta s/v$ in all cases.

5. Conclusion

We studied the interaction between mass and beam or rod while the former travels along the latter. We first considered a stiff beam undergoing only small deflections. The motion of the mass is then unaffected by the beam vibrations. We showed that the mass triggers small vibrations in the beam. For the case of a more flexible rod undergoing large deformations we then developed an efficient numerical scheme based on Cosserat theory using the generalised α-method for both spatial and temporal discretisation. The method is found to have very good convergence and stability properties (with tunable numerical damping). It can handle discontinuities in the force due to a point load well. Application to a few arch problems shows that a moving load has a stabilising effect on the, otherwise statically unstable, structure, both

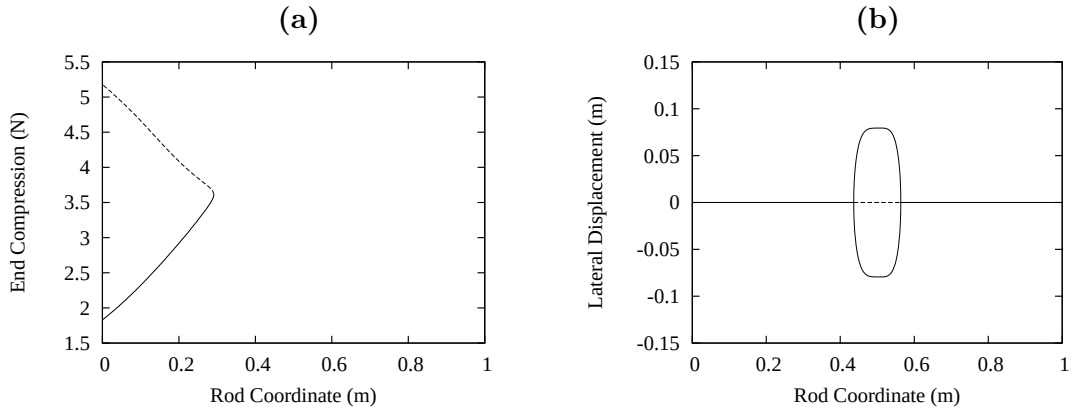

Figure 4. Bifurcation diagrams for the shallow (a) and deep (b) arch under quasistatic load F. Panel (a), showing the end compression $|\boldsymbol{n}(L) \cdot \boldsymbol{k}|$ against the rod coordinate σ for $F = 2.0\,\mathrm{N}$, reveals a fold at $\sigma = 0.291639\,\mathrm{m}$, while panel (b), showing the lateral end displacement x against σ for $F = 3.8\,\mathrm{N}$, reveals a pitchfork bifurcation at $\sigma = 0.436347\,\mathrm{m}$ followed by a reverse pitchfork bifurcation at $\sigma = 0.563653\,\mathrm{m}$. Solid branches are stable, dashed branches are unstable.

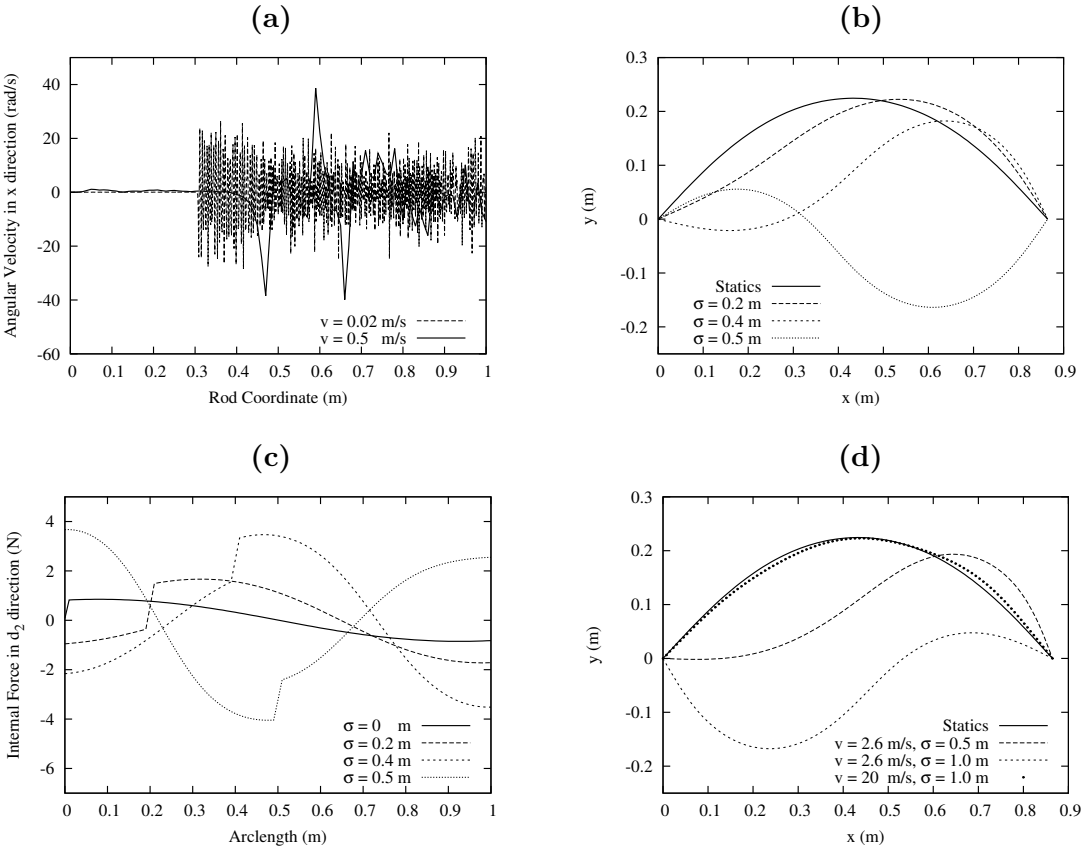

Figure 5. (a) Angular velocity $\boldsymbol{\omega}(L) \cdot \boldsymbol{i}$ about the hinge at $s = L$ as a function of the rod coordinate σ showing delayed buckling as the speed v is increased. (b) Arch shapes at various rod coordinates σ for $v = 0.5\,\mathrm{m/s}$, the last one, at $\sigma = 0.5$, after collapse has occurred. (c) Force component $n_2 = \boldsymbol{n} \cdot \boldsymbol{d}_2$ as a function of arclength s showing the travelling step discontinuity due to the point load F. (d) Arch shapes at higher speeds with collapse suppressed. ($F = 2.0\,\mathrm{N}$.)

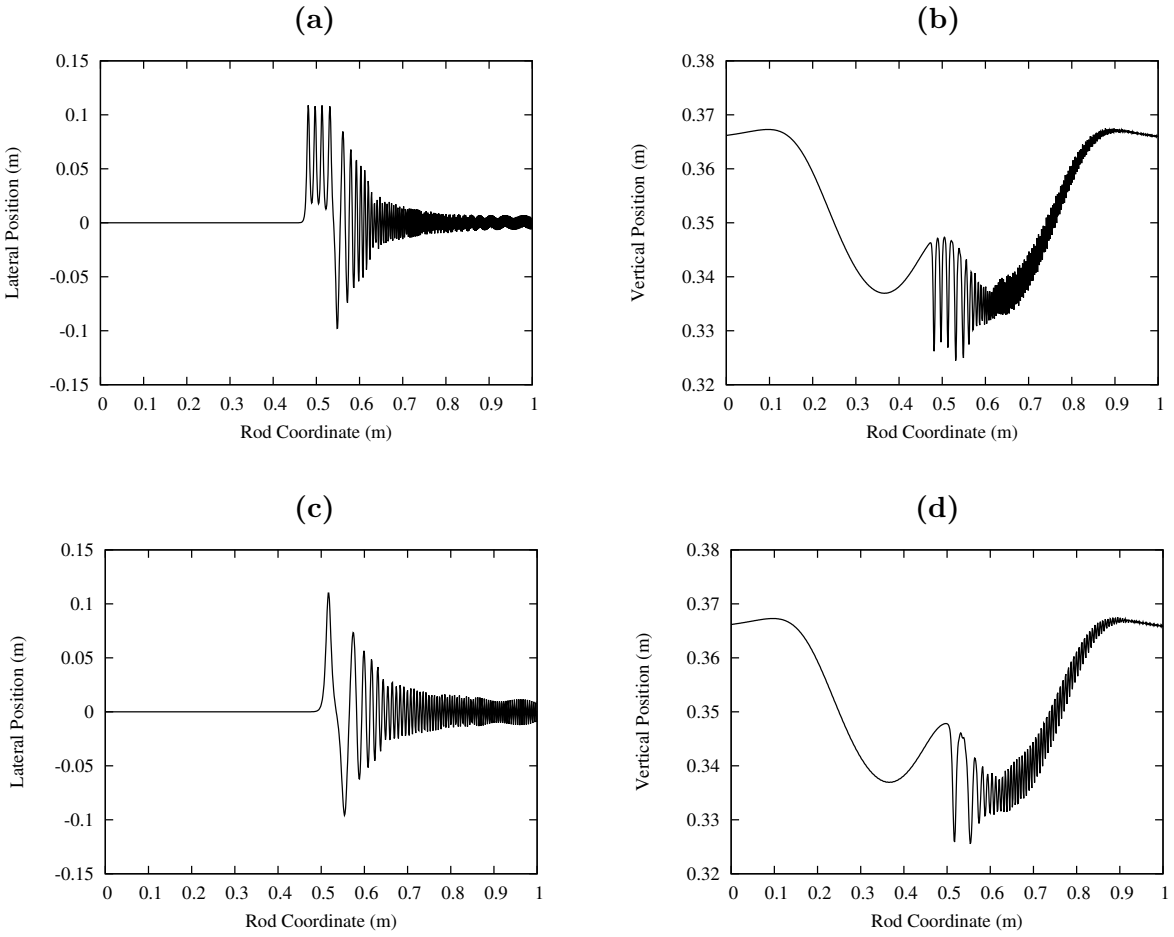

Figure 6. Lateral (x) and vertical (y) position of the deep arch with moving load at speeds $v = 0.005\,\mathrm{m/s}$ (a,b) and $v = 0.01\,\mathrm{m/s}$ (c,d). ($F = 3.8\,\mathrm{N}$.)

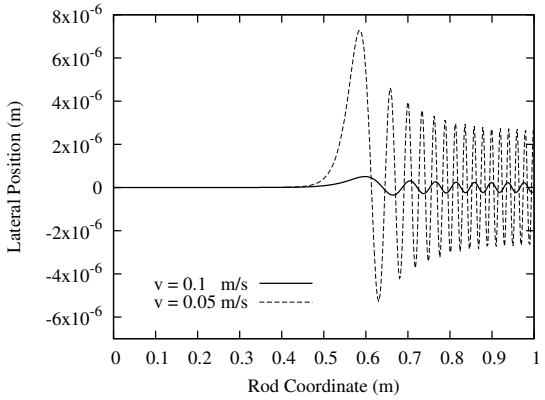

Figure 7. Lateral position x of the deep arch under a load travelling at higher speeds v, showing the stabilising effect of higher speeds. ($F = 3.8\,\mathrm{N}$.)

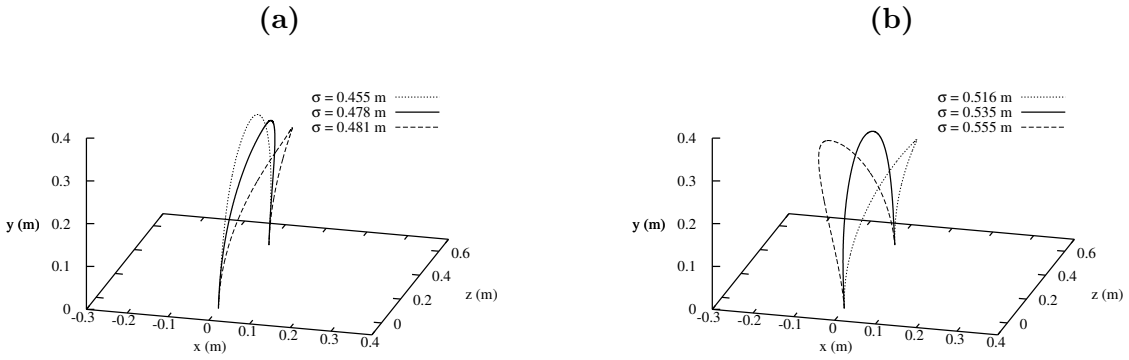

Figure 8. 3D shapes of the deep arch with moving load at different speeds: (a) $v = 0.005\,\mathrm{m/s}$, (b) $v = 0.01\,\mathrm{m/s}$. Shapes are shown at three different rod coordinates. ($F = 3.8\,\mathrm{N}$.)

for in-plane (collapse) instability, for a shallow arch, and for out-of-plane (flop) instability, for a deep arch. In many large-deformation applications of structures carrying a moving mass the mass will move autonomously along the cable, with a varying speed that depends on the local shape and velocity of the cable or arch. In future work we will investigate this two-way coupling between the dynamics of the cable and the mass.

References

[1] Wang P K C and Wei J 1987 Vibrations in a moving flexible robot arm, *J. Sound Vibr.* **116** 149–160
[2] Dwivedy S K and Eberhard K 2006 Dynamic analysis of flexible manipulators, a literature review, *Mech. Mach. Theory* **41** 749–777
[3] Ouyang H 2011 Moving-load dynamic problems: A tutorial (with a brief overview), *Mech. Syst. Signal Proc.* **25** 2039–2060
[4] Fryba L 1972 *Vibration of Solids and Structures under Moving Loads* (Groningen: Noordhoff)
[5] Sadiku S and Leipholz H 1987 On the dynamics of elastic systems with moving concentrated masses, *Arch. Appl. Mech.* **57** 223–242
[6] Ting E C, Genin J and Ginsberg J H 1974 A general algorithm for moving mass problems, *J. Sound Vibr.* **33** (1974) 49–58
[7] Ryu B J, Lee J W, Yim K B and Yoon Y S 2005 Dynamic behaviors of an elastically restrained beam carrying a moving mass, J. Mech. Sci. Technol. **20** 1382–1389
[8] Siddiqui S A Q, Golnaraghi M F and Heppler G R 2003 Large free vibrations of a beam carrying a moving mass, *Int. J. Non-Lin. Mech.* **38** 1481–1493
[9] Wu J J and Whittaker A R 1999 The natural frequencies and mode shapes of a uniform cantilever beam with multiple two-dof spring-mass systems, *J. Sound Vib.* **227** 361–381
[10] Zhao X W, Hu Z D and van der Heijden G H M 2015 Dynamic analysis of a tapered cantilever beam under a travelling mass, *Meccanica* **50** 1419–1429
[11] Antman S S 2005 *Nonlinear Problems of Elasticity* (2nd ed.) (New York: Springer)
[12] Goyal S, Perkins N C and Lee C L 2008 Non-linear dynamic intertwining of rods with self-contact, *Int. J. Non-Lin. Mech.* **43** 65–73
[13] Sobottka G, Lay T and Weber A 2008 Stable integration of the dynamic Cosserat equations with application to hair modeling, *J. WSCG* **16** 73–80
[14] Chung J and Hulbert G M 1993 A time integration algorithm for structural dynamics with improved numerical dissipation – the generalized-α method, *J. Appl. Mech.* **60** 371–375
[15] Nowak U and Weimann L 1991 A family of Newton codes for systems of highly nonlinear equations, *Technical Report TR-91-10* (Konrad-Zuse-Zentrum für Informationstechnik Berlin)
[16] Murray R M, Li Z X and Sastry S S 1994 *A Mathematical Introduction to Robotic Manipulation* (Boca Raton: CRC Press)
[17] Xu F Y, Wang L, Wang X S and Jiang G P 2013 Dynamic performance of a cable with an inspection robot: analysis, simulation, and experiments, *J. Mech. Sci. Technol.* **27** 1479–1492
[18] Olsson M 1991 On the fundamental moving load problem, *J. Sound Vibr.* **145** 299–307